ACSNANO

www.acsnano.org

ARTICLE

Transient Lattice Response upon Photoexcitation in $CuInSe_2$ Nanocrystals with Organic or Inorganic Surface Passivation

Samantha M. Harvey, Daniel W. Houck, Matthew S. Kirschner, Nathan C. Flanders, Alexandra Brumberg, Ariel A. Leonard, Nicolas E. Watkins, Lin X. Chen, William R. Dichtel, Xiaoyi Zhang, Brian A. Korgel, Michael R. Wasielewski, and Richard D. Schaller*

Cite This: *ACS Nano* 2020, 14, 13548–13556

Read Online

ACCESS | Metrics & More | Article Recommendations | Supporting Information

ABSTRACT: **$CuInSe_2$ nanocrystals offer promise for optoelectronics including thin-film photovoltaics and printed electronics. Additive manufacturing methods such as photonic curing controllably sinter particles into quasi-continuous films and offer improved device performance. To gain understanding of nanocrystal response under such processing conditions, we investigate impacts of photoexcitation on colloidal nanocrystal lattices via time-resolved X-ray diffraction. We probe three sizes of particles and two capping ligands (oleylamine and inorganic S^{2-}) to evaluate resultant crystal lattice temperature, phase stability, and thermal dissipation. Elevated fluences produce heating and loss of crystallinity, the onset of which exhibits particle size dependence. We find size-dependent recrystallization and cooling lifetimes ranging from 90 to 200 ps with additional slower cooling on the nanosecond time scale. Sulfide-capped nanocrystals show faster recrystallization and cooling compared to oleylamine-capped nanocrystals. Using these lifetimes, we find interfacial thermal conductivities from 3 to 28 MW/(m^2 K), demonstrating that ligand identity strongly influences thermal dissipation.**

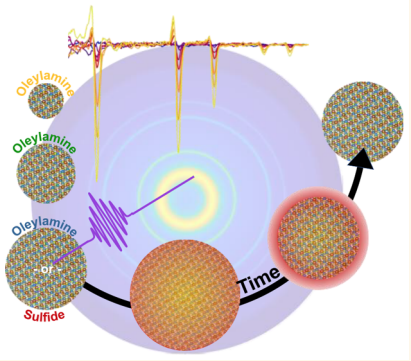

KEYWORDS: *time-resolved X-ray diffraction, $CuInSe_2$, ligand, melting, heat dissipation*

Colloidally synthesized semiconductor nanocrystals (NCs) offer the prospect of electronically tailorable inks, which can be deposited as thin films for light-emitting diodes[1] or photovoltaics.[2] Significant interest exists in passive or active patterning of these materials to obtain superlattices[3,4] or printed electronics.[5,6] Because of quantum confinement of electron–hole pairs (often referred to as excitons regardless of binding energy), NCs can exhibit optoelectronic properties that differ substantially from bulk counterparts and are electronically tunable through size and shape.[7,8] At the same time, reducing particle size to the nanoscale also impacts thermal behavior and elevates the importance of interfacial phenomena. For instance, NCs exhibit highly active surfaces and substantial melting point depression compared to the bulk because of high surface energy.[9−12] Thus, particles can, desirably or undesirably, sinter together into more spatially extended, bulk-like solids under temperature elevation or local methods such as pulsed laser annealing.[13−17] In the latter of these approaches, above-bandgap optical excitation produces intraband-relaxation-induced heating as electronic carriers cool via phonon scattering,[18,19] and for excitation regimes that produce multiple excitons per particle, Auger recombination annihilates excitons to produce hot carriers that subsequently impart thermal energy into the lattice.[20,21] Investigations into the effects of heating in NCs significantly lags behind research on their synthesis and optoelectronic properties. Namely, the correlation of excitation fluence, effective lattice temperature, and rates of cooling remain poorly characterized.[22−24] With improved understanding of these behaviors, the physical response of NCs can be better predicted and controlled.

$CuInSe_2$ NCs in particular are of interest for their solution processability and bulk-phase near-infrared bandgap (1.02 eV at 298 K) comparable to that of silicon (1.1 eV).[25−28] Additionally, this composition is a less toxic alternative to

Received: July 5, 2020
Accepted: September 11, 2020
Published: September 11, 2020

https://dx.doi.org/10.1021/acsnano.0c05553
ACS Nano 2020, 14, 13548–13556

common semiconductor NCs such as CdSe or $CH_3NH_3PbI_3$.[29] These properties have led to their incorporation into thin film solar cells. $CuInSe_2$ NCs can be drop cast[30−33] or sintered to produce uniform, highly conductive, bulk-like thin film photovoltaics,[34,35] with record efficiencies up to 15% for bulk[36] and 7% for NCs.[27,37,38] Sintering is often performed either under sustained elevated temperatures in the presence of selenium vapor or by rapid photonic curing,[17,39] where the latter offers the prospect of retaining quantum confinement while increasing conductivity. Another broadly researched method for improving devices is substitution of the highly insulating, synthetic ligands for small inorganic ions that improve carrier mobility between the NC cores by reducing spatial separation, thus facilitating charge transport.[40−43]

Here, we examine the structural responses to photoinduced thermal effects in $CuInSe_2$ NCs as a function of particle size, as well as the impacts of altering surface chemistry from the insulating organic ligand, olelyamine (OLAm), to a short inorganic ligand, S^{2-}. Time-resolved X-ray diffraction (TR-XRD) allows us to directly monitor the effects of optical excitation on the crystalline lattice as functions of both laser fluence and time delay between excitation and X-ray pulses. From this technique, we can monitor the effects of rapid deposition of thermal energy upon intraband relaxation and Auger recombination.[22,24,44,45] We find size-dependent melting thresholds and recrystallization dynamics where larger NCs require more absorbed photons (and, thus, excitons) to melt and longer to return to equilibrium. Exchange to S^{2-} ligands does not appreciably impact melting threshold; however, the sulfide-capped NCs recover much more quickly than the OLAm counterparts. Fitted cooling times relate order-of-magnitude higher interfacial thermal conductivity for the S^{2-} ligand. Finally, we perform temperature-dependent, static X-ray diffraction calibrations to quantify transient lattice expansion as well as to determine effective lattice melting temperature.

RESULTS AND DISCUSSION

We synthesized three $CuInSe_2$ NC ensembles with average diameters of 3.4, 5.4, and 10.8 nm, herein referred to as small, medium, and large particles, using published methods.[27,46] The surfaces of these NCs were passivated during synthesis with OLAm ligands and dispersed in dodecane for XRD experiments. As described in the Experimental Section, a portion of the large NCs were separately ligand-exchanged using Na_2S to replace the surface functionalization with sulfide anions (S^{2-}), a common inorganic capping agent,[42] and dispersed as a stable colloidal suspension in more polar dimethylformamide (DMF). Fourier transform infrared (FTIR) spectra in the Supporting Information of the samples before and after ligand exchange confirm complete replacement of OLAm by S^{2-} (Figure S1). The static XRD patterns of all four samples appear in Figure 1a and match calculated reflections of the chalcopyrite crystal structure.[47] As the NCs decrease in size, diffraction features increase in width because of Scherrer broadening (Figure S4). Both large NC samples exhibit similar diffraction peak line widths, with a slight increase in full-width half-maximum (fwhm) for the S^{2-} sample indicating that the ligand exchange caused minimal reduction in size. Transmission electron microscopy (TEM) evaluation of particle size (Figure S3) also shows an average diameter of 10.2 nm for the large, S^{2-} sample compared to 10.8 for the OLAm sample with overall shape unchanged. Figure 1b displays images of the

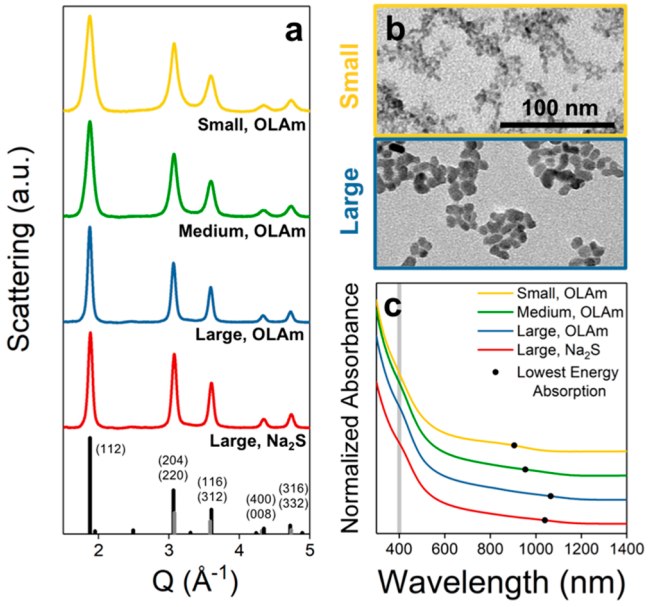

Figure 1. Static characterization of $CuInSe_2$ NCs: (a) Static X-ray diffraction patterns of the four studied samples displaying the labeled chalcopyrite diffraction peaks. (b) TEM images of the small (3.4 ± 0.9 nm diameter, upper panel) and large (10.8 ± 3.1 nm, lower panel) NCs capped with olelyamine. (c) Normalized and offset steady-state absorption spectra with marker denoting the lowest-energy absorption peak and gray vertical bar indicating optical pump excitation wavelength for the TR-XRD experiments (400 nm).

small and large OLAm-capped NCs, which are approximately spherical though they tend to aggregate when dried on a grid (electron microscopy of all samples appears in Figure S3). Steady-state absorption spectra of the samples in Figure 1c show broad band-edge absorption, characteristic of this material composition, with an onset in the near-infrared that extends through the visible. The lowest-energy transition for each sample is marked with a circle, as well as the laser excitation wavelength (400 nm, gray bar) used in TR-XRD experiments. We note that the transition for the large S^{2-} is bluer than that of the OLAm sample due to the difference in size.

We performed TR-XRD using 1.6 ps, 400 nm pump pulses from the frequency doubled output of an amplified Ti:sapphire laser and 11.7 keV X-ray probe pulses at Beamline 11-ID-D of the Advanced Photon Source (Argonne National Laboratory). The combined instrument response function was 79 ps. NCs suspended in dodecane (DMF for S^{2-} exchanged particles) were rapidly flowed through a degassed, recirculating liquid jet. Upon controlled-fluence optical excitation, lattice heating and expansion of the NCs can produce symmetric derivative-like features in the differenced XRD patterns as peaks shift to lower Q values, whereas transient disordering or melting results in negative features due to reduced diffraction intensity in comparison to static XRD[44,45] (see the Supporting Information for more experimental information and differenced diffraction pattern examples). With increasing laser fluence, j, the average number of photogenerated electron−hole pairs per excited NC, $\langle N \rangle = \sigma j$, increases in accordance with the size-dependent absorption cross-section, σ (Table S2), which results in both single-picosecond intraband relaxation-derived heating of initially hot excitons as well as tens-of-picosecond, non-

https://dx.doi.org/10.1021/acsnano.0c05553
ACS Nano 2020, 14, 13548−13556

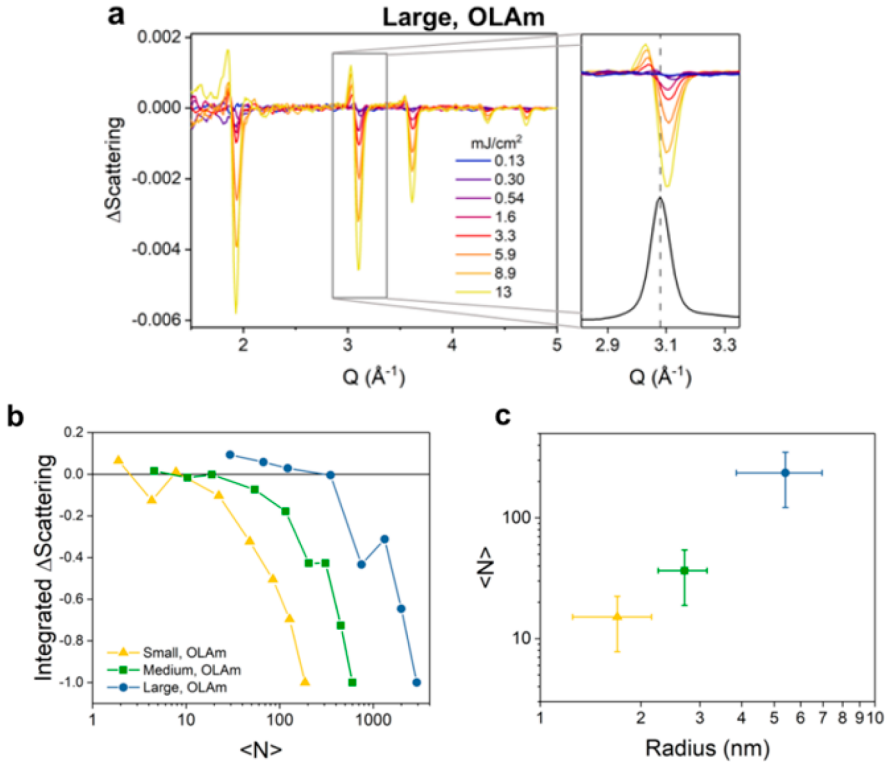

Figure 2. Fluence-dependent TR-XRD data measured 40 ps after excitation. (a) Pump-on vs pump-off differences in diffraction for the large, OLAm NCs show lineshapes that become asymmetric at higher indicated fluences, indicative of both heating and melting. To the right is a zoomed-in view of the (220)/(204) feature with the static XRD (black). The gray dashed line corresponds to the peak position prior to excitation. (b) Integration in Q-space of the (220)/(204) and (116)/(312) peaks relates net reduced diffraction and loss of crystallinity (melting). (c) Comparison of radius to melting threshold for the three sizes.

Table 1. Dynamics Lifetimes, Melting Thresholds, And Melting Temperatures

sample (diameter, capping ligand)	τ_1 (ps)	τ_2 (ns)	melting threshold (<*N*>)	melting point from power dependence (°C)	melting point from dynamics (°C)
small (3.4 nm, OLAm)	90 ± 27	2.3 ± 1.3	7.8–22	-	-
medium (5.4 nm, OLAm)	136 ± 29	2.4 ± 1.1	19–54	455 ± 20	325 ± 50
large (10.8 nm, OLAm)	201 ± 57	2.5 ± 1.2	122–350	615 ± 60	525 ± 50
large (10.2 nm, S^{2-})	207 ± 42		103–297		

radiative, multiexciton Auger recombination–derived heating.[18,34]

For each of the three OLAm NC samples, we measured fluence-dependent TR-XRD signals, which appear in Figure 2a for the largest NC sample at a pump–probe time delay of 40 ps (Figure S6 shows data for small and medium NCs). At lower laser fluences, symmetric derivative lineshapes appear, with increased scattering at lower *Q*, relating NC lattice expansion. As *j* increases, the peaks become asymmetric with a larger amplitude negative component, consistent with the onset of transient disordering or melting. We presume that melting occurs over the volume of the nanocrystal and not solely at the surface based on the line shape, as surface melting would result in substantial Scherrer broadening from the smaller crystalline core of the NC. Weak trends associated with Debye–Waller effects that relate larger diffraction losses in higher *Q* features are observed (described in the Supporting Information).[48] Integration in *Q*-space of the (204)/(220) and (116)/(312) peaks, shown in Figure 2b as a function of ⟨*N*⟩, effectively nullifies the symmetric derivative (lattice expansion) features and therefore conveys transient disordering (melting) behavior of these materials. Presented data are normalized to allow easier comparison. For all three samples, the melted fraction increases with ⟨*N*⟩. Table 1 shows melting threshold values and further explanation appears in the Supporting Information. Even higher powers caused irreversible degradation of the samples. Figure 2c plots the melting threshold of the three OLAm samples versus radius on a log–log scale showing the shift in threshold to higher ⟨*N*⟩ ranges as size increases. Similar to previous studies of CdSe NCs,[45] we observe that a larger number of photogenerated excitons per particle are needed to achieve transient disordering in larger $CuInSe_2$ NCs. This trend, which already incorporates effects of absorption cross-section, relates to the higher specific heat of larger NCs as well as changing fractional surface energy.[12,49] When corrected for volume, the average number of excitons needed to melt is fairly consistent across the three samples (Table S3), further evidence that melting is occurring throughout the NC and not just at the surface.

We analyzed picosecond to microsecond dynamics of TR-XRD signals for the three particle sizes to determine thermal dissipation rates. In this comparison, samples were excited above the melting threshold and differenced diffraction patterns for the samples at several time delays appear in

https://dx.doi.org/10.1021/acsnano.0c05553
ACS Nano 2020, 14, 13548–13556

Figures 3a–c. Similar to the power dependence at high flux, the early time points exhibit asymmetric peak shapes,

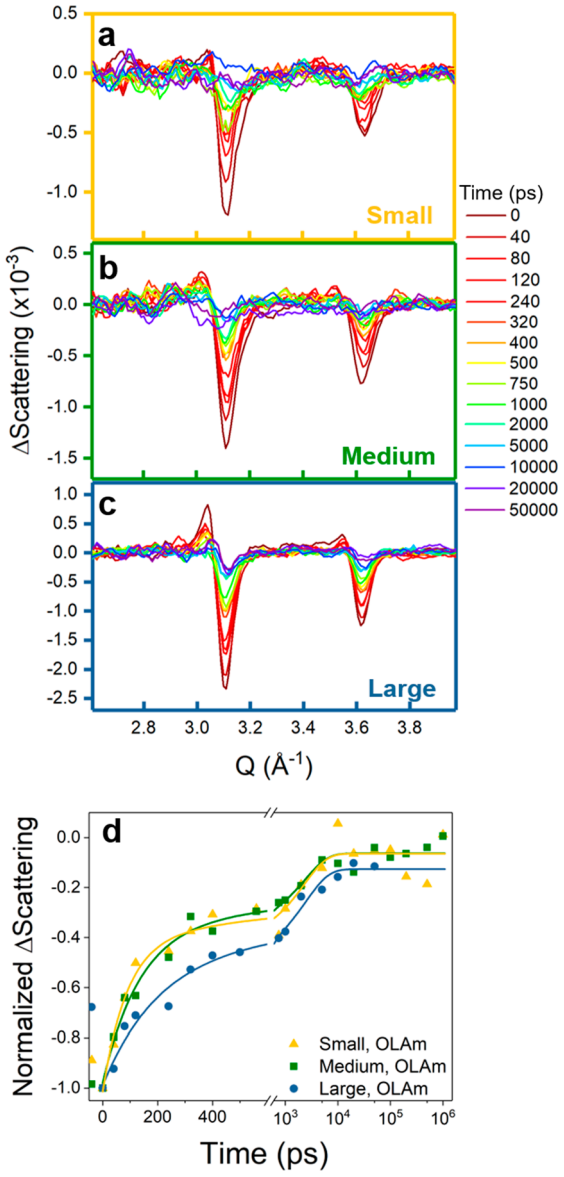

Figure 3. TR-XRD dynamics at 5.9 mJ/cm^2. (a–c) Differenced spectra for the large, medium, and small OLAm NCs as a function of time delay showing the region around the (220)/(204) and (116)/(312) peaks. (d) Integration of the negative component of the (220)/(204) and (116)/(312) peaks for the three different size OLAm-capped NCs. Dynamics are a convolution of both recrystallization and cooling that cause a biexponential recovery. Early times show a clear size-dependent trend to recrystallization within the first several hundred picosecond time window. Late times (note axis break) are characterized by continued cooling of the NCs that occurs on the nanosecond time scale.

suggesting a mixture of heated and melted NCs. In order to analyze the dynamics, we integrated only the negative transient signals of the (204)/(220) and the (116)/(312) peaks, shown in Figure 3d, as integration of the entire transient feature increased noise in the analysis. Such evaluation does not separate the melting vs lattice-expansion component. Though the instrument lacks sufficient time-resolution to evaluate the melting process, two distinct recovery regions are apparent in these integrated dynamics and necessitate biexponential fitting (τ_1 and τ_2, details of the fitting process appear in the Supporting Information). The more rapid τ_1 region corresponds to both NC recrystallization and cooling that is on the order of hundreds of picoseconds and shows a size-dependent trend among the three samples, with faster recovery for the smaller particles.[22,49,50] The slower τ_2 region is marked by continued NC cooling and lattice reversion back toward the original volume. This occurs on a nanosecond time scale in the range of ~2 ns.[22,49,50] Although a slight size-dependent trend is evident, the reduced signal level at late times does not allow us substantial additional insights; however, local heating of ligands and proximal solvent could slow apparent cooling. Further support for two regimes derives most clearly from the dynamics of the large NCs in Figure 3c, where the asymmetric line shape at early times transforms into a more symmetric derivative that then continues to decay in intensity.

In order to discern transient changes in effective lattice temperature in time-resolved signals, we performed static X-ray diffraction for equilibrium sample temperatures ranging from 25 to 170 °C. As seen in Figure 4a, b for the largest NCs, diffraction peaks shifted to lower Q as expected upon static temperature elevation, though changes are small (<0.01 Å^{-1} upon changing from 25 to 170 °C). After baseline subtraction, the peaks were fit to pseudo-Voigt lineshapes, which are commonly implemented for XRD patterns.[51] We were able to determine the change in lattice parameters (a and c) as well as particle volume (Figure 4c) for the medium and large NC samples. Reliable fitting of the smallest NCs was imprecise because of the broad and asymmetric lineshapes. We find that NC lattices of the large and medium sizes expand more than the bulk over the probed temperature range.[52] Bulk $CuInSe_2$ has nonlinear thermal expansion, but by 160 °C, we find that the medium and large samples had expanded by 0.57 and 0.44%, respectively, compared to the bulk expansion of 0.13%. Similarly, the medium NCs expanded more than the large, likely related to increased surface energy per particle.[53−55] Although we were unable to measure thermal expansion for the smallest sample, we anticipate that it would have an even larger percentage of expansion than the medium NCs.

On the basis of the temperature-dependent XRD measurements, we estimate changes in effective lattice temperature as a function of pump–probe time delay (Figure 4d) and laser fluence (Figure 4e) for the large and medium OLAm NC samples. The effective lattice temperatures derived from the kinetics show fairly constant temperatures at early times after excitation, commensurate with the τ_1 time component. As discrete NCs are recrystallizing during this time window, we suggest that lattice heat of fusion partially negates cooling as the lattice orders, consistent with a phase transition. There is then a more pronounced decrease in temperature at later times corresponding solely to heat dissipation. Averaged temperatures at early times appear in Table 1. Fluence-dependent data at high powers (Figure 4e) show similar plateaus in effective lattice temperature. Here, proximity to the apparent melting threshold results in leveling-off of the temperature increase with fluence, in particular because only the fractional population of remaining crystalline lattices continue to strongly diffract. From the highest fluences examined, we estimate a nonequilibrium melting temperature of ~455 (±20) °C for the medium NCs and ~615 (±60) °C for the large NCs. Although higher than those found from the dynamics, both analyses show the same trend. Similar to other NC compositions, these

https://dx.doi.org/10.1021/acsnano.0c05553
ACS Nano 2020, 14, 13548–13556

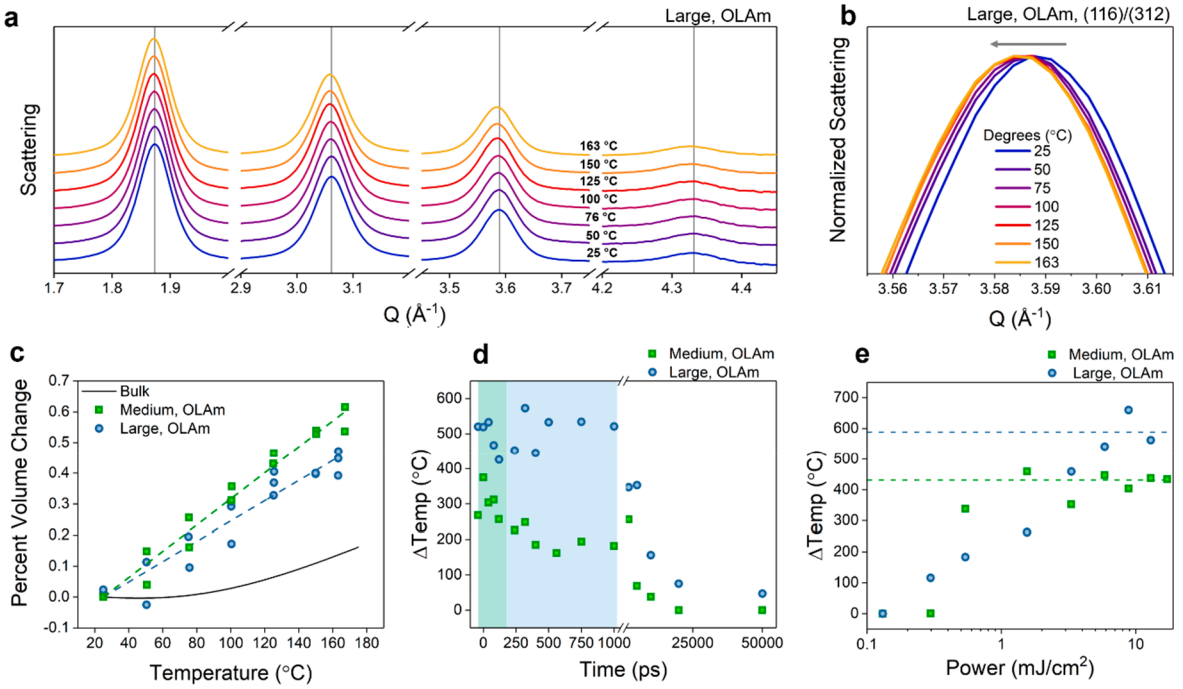

Figure 4. Temperature-dependent static XRD. (a) Large, OLAm NC XRD as a function of temperature shows shifts to lower Q values. (b) Normalized, zoomed-in XRD of the (116)/(312) diffraction peak showing shift with temperature. (c) Fits of these peaks relate the change in lattice volume as a function of temperature for the medium and large OLAm NCs. Dashed lines shown are meant to guide the eye. The thermal expansion of bulk $CuInSe_2$ is plotted in black for comparison. (d) Time-dependent (at j = 5.9 mJ/cm^2) and (e) fluence-dependent (at t = 40 ps) changes in temperature derived from TR-XRD for the large and medium OLAm NCs. Data were fit using parameters from static temperature-dependent XRD to correlate peak shift with temperature. At early times in d, the temperature remains fairly constant over τ_1 lifetimes, suggesting recrystallization processes. Shaded areas represent constant temperature. In e, transient signals at larger fluences lack a systematic increase in effective temperature with fluence, suggesting the NCs undergo disordering (cease diffracting strongly) in this range.

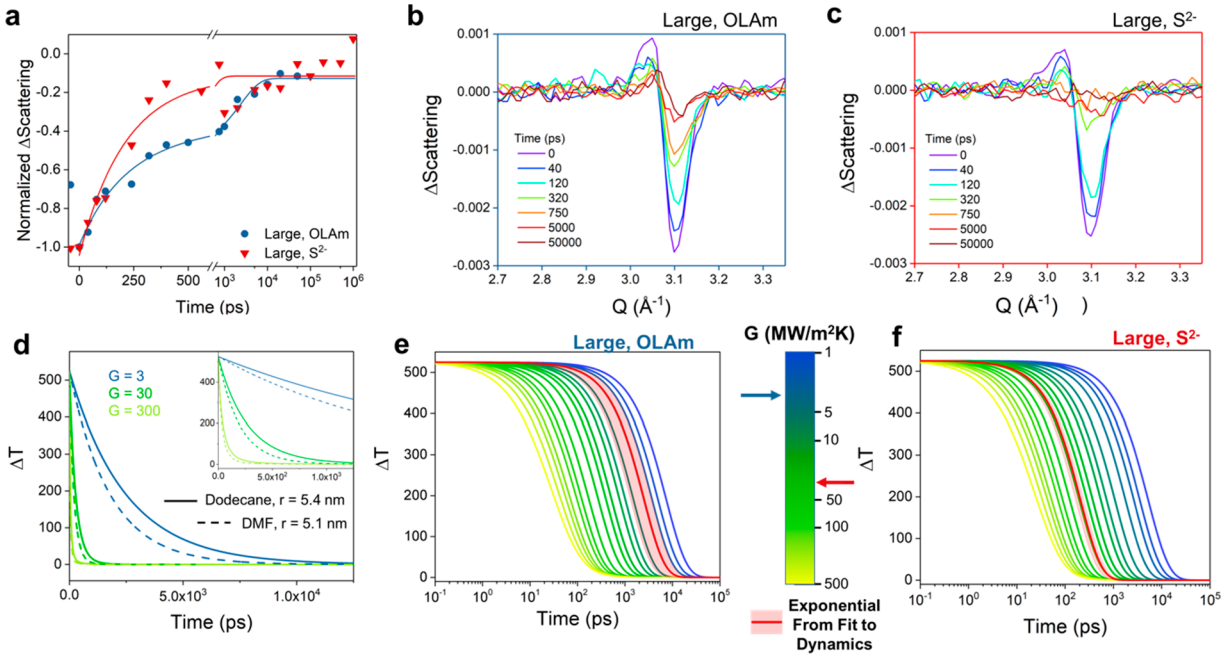

Figure 5. Effect of S^{2-} ligand on dynamics. (a) The S^{2-} sample recovers with only one exponential in the dynamics that is similar to the τ_1 lifetime of the OLAm sample. Transient diffraction signals as a function of time delay of the (220)/(204) feature in the (b) OLAm and (c) S^{2-} samples showing different recrystallization and cooling behavior. (d) Effects of solvent and radius on G. The S^{2-} sample has a reduced diameter and different solvent, both of which cause faster cooling, but cannot explain the order of magnitude difference in lifetime. (e, f) Calculated functions of G with the experimentally derived exponential functions overlaid for OLAm and S^{2-}, respectively. Ligand exchange from OLAm to S^{2-} results in a drastic increase in G from ~3 to ~28 MW/(m^2 K).

https://dx.doi.org/10.1021/acsnano.0c05553
ACS Nano 2020, 14, 13548−13556

melting points are size dependent and appreciably lower than the equilibrium bulk-phase melting point (987 °C).[26]

Lastly, we exchanged the native OLAm ligand on the largest NCs for S^{2-} (using Na_2S) and repeated the measurements noted above. Figures S6 shows that the melting threshold of the S^{2-} sample is nearly unchanged from the OLAm sample, with a very slight reduction. Seeing as the TEM images and static X-ray diffraction showed a slight decrease in the diameter of the NC after ligand exchange, we attribute the subtle difference to a size effect, although surface energy will also differ for the different ligands. We plot the melting threshold vs radius in Figure S7. When fitting the OLAm samples to a power law, we find that the S^{2-} sample agrees reasonably with the fit, confirming that the change in ligand identity in this instance does not distinctly affect the melting threshold.

Recovery dynamics, however, are markedly different between the two ligand types for the large NCs as shown in Figure 5a. The inorganically terminated sample presents only a single exponential recovery component that is nearly identical to the τ_1 component of the OLAm sample. Figure 5b,c shows that the (204)/(220) and (116)/(312) features of the S^{2-} sample recover rapidly as compared to the OLAm sample. The lack of a second, slower component suggests that the inorganically capped NCs not only recrystallize within this time, but also cool almost completely. Together, the fluence dependence and dynamics suggest negligible impact of S^{2-} ligands on melting but accelerated cooling and recrystallization. Whereas several factors may influence the observed behavior, we suspect that thermal transport from the NC to solvent occurs more rapidly through the compact anionic ligands rather than the many-atom OLAm ligand, and that direct interactions between the NC surface and solvent more readily occur and facilitate cooling.

To explore whether these differences could be attributed to the ligand and not the different solvent or slight reduction in NC diameter, we modeled the cooling of the particles using established thermal dissipation equations.[56] Figure 5d shows effects that both solvent and radius have on the cooling rates for three different values of interfacial thermal conductivity (G). Although DMF (rather than dodecane) and the slightly smaller particle radius of the S^{2-} sample do cause a reduction in the cooling lifetime, such effects are less significant than the order-of-magnitude difference that we observe. We then used this model to approximate G values for both large samples. Figure 5e,f displays a variety of G values for the large samples with the lifetime of cooling derived from the fits of the TR-XRD overlaid in red. From this comparison, we find G values of 3 and 28 MW/(m^2 K) for the OLAm sample and the S^{2-} samples, respectively. Such values are comparable to those determined theoretically for other semiconductor NC compositions.[57,58]

Ligand selection is critical to implementation of a given nanocrystal composition in applications owing to significant effects on solution processing and electrical conductivity.[59−62] Ligand identity impacts the rate of thermalization as observed in this pulsed excitation mode with isolated NCs dispersed in solvent. The temperature−time profile of a film of nanocrystals, whether in a light-emitting application or additive manufacturing process, is influenced not only by the rate of thermalization, but also on thermal properties (heat capacity, thermal transport) of surrounding or proximal media. For continuous- or high-frequency excitation, interfacial thermal conductivity impacts the rate at which the NC together with the surroundings will exchange heat and establish a quasi-equilibrium, which would occur more rapidly here for the inorganic ligand. Several effects play a role in photonic curing or sintering, such as the available thermal energy, the time available for interparticle bond formation, NC packing density, ligand identity, fractional ligand coverage, surface binding energy, and any ligand chemical processes. Here, for instance, the compact S^{2-} inorganic ligand offers close NC proximity although the NC core can cool more rapidly than the studied organic ligand. From this analysis, we suggest that ligand identity yields significant consequences for thermal dissipation at interfaces of these materials and due to facile routes to manipulate composition, a perhaps highly effective tool for controlling such processes.

CONCLUSION

In conclusion, we have performed TR-XRD and temperature-dependent static XRD experiments to probe photoinduced heating and melting in $CuInSe_2$ NCs as functions of both particle size and ligand identity. We found NC size dependence in both melting threshold and recrystallization/cooling dynamics. In addition, we found that the NC size affects lattice expansion with static temperature elevation and melting temperature in TR-XRD. Using this approach, we were able to study the effects of ligand identity on lattice response and thermal dissipation. Exchange of long, bulky OLAm ligands to short sulfide anions did not alter the photoinduced disordering threshold, but appreciably impacted cooling and recrystallization lifetimes. We were also able to obtain interfacial thermal conductivity values for the two different ligand terminations. Taken together, these findings suggest several means exist to manipulate nanoparticle phase and thermal profile. Overall the amount of energy deposited (which here is pulsed, but could also be continuously input), as well as particle size, surface termination, and surroundings physically alter the nanocrystalline material in an appreciable manner.

METHODS AND EXPERIMENTAL SECTION

Synthesis of $CuInSe_2$ Nanocrystals. Five millimoles of CuCl (0.49 g), 5 mmol of $InCl_3$ (1.11 g), 10 mmol of Se (0.79 g), and 40 mL of oleylamine were loaded into a 100 mL three-neck flask in a nitrogen-filled glovebox. The flask was sealed and transferred onto a Schlenk line. The reaction mixture was held under vacuum (<200 mTorr) at 110 °C for 12 h to degas and allow precursor complexes to form. The flask was then filled with nitrogen and heated to a reaction temperature of 200, 220, or 240 °C for 10 min, with higher reaction temperatures yielding larger nanocrystals (NCs). The heating mantle was then removed, and the reaction mixture was allowed to cool below 60 °C.

Next, the NCs were purified with two precipitative isolation steps. The crude reaction solution was transferred into centrifuge tubes and 40 mL of ethanol was added to precipitate the NCs. The solution was centrifuged at 2600 rcf for 10 min and the clear supernatant was discarded. The precipitated NCs were redispersed in 10 mL of toluene and centrifuged again at 2600 rcf for 10 min. The well-dispersed NCs in the supernatant were transferred to another centrifuge tube and 10 mL of ethanol was added. The solution was centrifuged again at 2600 rcf for 10 min and the clear supernatant was discarded. The purified NCs were dispersed once more in 5 mL of toluene and centrifuged a final time at 2600 rcf to remove any poorly capped particles. The nanocrystal solution was then dried by rotary evaporation, weighed, and transferred to a nitrogen-filled glovebox. Finally, the NCs were dissolved in anhydrous toluene at a concentration of 100 mg/mL and stored in a glove box. In this

https://dx.doi.org/10.1021/acsnano.0c05553
ACS Nano 2020, 14, 13548−13556

state, the NCs retain colloidal stability for months to years. For X-ray diffraction experiments, NCs were dried under nitrogen and dispersed in dodecane.

Na_2S Ligand Exchange. In a nitrogen-filled glovebox, 260 mg (3.33 mmol) Na_2S was dissolved in 3 mL of formamide. Three milliliters of $CuInSe_2$ NCs dissolved in toluene at a concentration of 100 mg/mL was then added to the Na_2S solution, which formed a biphasic mixture. The solution was stirred for 2 h, during which time the NCs transfer from the toluene phase to the formamide phase. The clear toluene phase is then decanted. Clean toluene was then added, the solution was shaken, and the toluene was decanted again to remove any residual oleylamine ligand. This toluene rinse was repeated 2 more times. Next, the solution was centrifuged at 2600 rcf for 5 min. The clear supernatant was discarded, and the NCs were dispersed in 5 mL of methanol. Five milliliters of toluene was then added to precipitate the NCs and the solution was centrifuged again at 2600 rcf for 5 min. The clear supernatant was discarded and the methanol/toluene precipitation procedure was repeated 2 more times, for a total of three precipitative isolation steps. The purified S^{2-}-capped NCs were then transferred into a nitrogen-filled glovebox and dispersed in anhydrous methanol, where they retained colloidal stability for months to years. The NCs were dried and dispersed in DMF prior to X-ray diffraction experiments. FTIR experiments confirmed complete ligand exchange from oleylamine to S^{2-} (Figure S1).

Steady-State Absorption. Steady-state absorption was measured with a Cary-5000 UV−Vis−NIR spectrophotometer. Samples were prepared by filling a 1 cm path length quartz cuvette with a dilute solution of $CuInSe_2$ NCs in toluene. All spectra were background-subtracted against the same quartz cuvette filled with toluene. The lowest-energy absorption for each sample was determined from transient absorption measurements (not shown) and the lowest-energy optical bleach signal indicated the minimum band-edge transition energy.

Static X-ray Diffraction. Static X-ray diffraction patterns of nanocrystal powders were acquired using a Rigaku R-axis spider diffractometer with an image plate detector and Cu Kα (λ = 1.54 Å) radiation source. Dried powder was suspended on a 0.5 mm nylon loop and was scanned for 10 min while rotating at 1°/s. The diffraction patterns were then integrated with the Rigaku 2DP powder processing program.

Transmission Electron Microscopy. TEM grids were prepared by drop casting a dilute solution of $CuInSe_2$ nanocrystals onto a carbon film mesh nickel grid acquired from Electron Microscopy Sciences. TEM images were then acquired with a FEI Tecnai Spirit Bio Twin with 80 kV accelerating voltage.

Temperature-Dependent X-ray Diffraction. NC samples were added to 1.5 mm borosilicate capillaries which were then placed in a heating cell with windows on both sides to allow for transmission of X-rays. A k-type thermocouple was docked into the heating cell to read real-time temperature and allow for adjustments via a PID controller. Samples were heated to the temperatures listed in the text, and allowed to equilibrate for 10 min, after which point 17 keV X-rays from a synchrotron source (Sector-5, DND-CAT, Argonne) irradiated the sample generating a diffraction pattern collected on three Pilatus 2M detectors. These detectors are two-dimensional in nature, so 1D plots of intensity with respect to q were generated by integrating the intensity of the diffraction signal azimuthally around the central point of origin.

Time-Resolved X-ray Diffraction. The setup for TR-XRD is described elsewhere.[44,45] During measurement, a reservoir of the NCs (~10−20 mL) were kept under nitrogen atmosphere. A peristaltic pump pulled sample from the reservoir and produced a thin jet of NCs (450 μm). This constantly flowing supply was then excited with a 400 nm laser (frequency doubled output of a Ti:sapphire laser, 10 kHz, 1.6 ps fwhm). After set time delays, X-ray pulses probed the sample (bunches from the Advanced Photon Source storage ring, 79 ps fwhm). X-ray diffraction was detected using a Pilatus 2M detector and radially integrated.

ASSOCIATED CONTENT

Supporting Information

The Supporting Information is available free of charge at https://pubs.acs.org/doi/10.1021/acsnano.0c05553.

Transmission electron microscopy images and sizing histograms, Debye−Waller effects, transient XRD and pump-intensity-dependent XRD of all samples, comparison of melting threshold between OLAm and S^{2-} passivation, temperature-dependent XRD for medium OLAm sample, fitting procedures and constants for temperature-dependent XRD, interfacial thermal conductivity (PDF)

AUTHOR INFORMATION

Corresponding Author

Richard D. Schaller − *Department of Chemistry and Institute for Sustainability and Energy at Northwestern, Northwestern University, Evanston, Illinois 60208, United States; Center for Nanoscale Materials, Argonne National Laboratory, Lemont, Illinois 60439, United States;* orcid.org/0000-0001-9696-8830; Email: schaller@northwestern.edu, schaller@anl.gov

Authors

Samantha M. Harvey − *Department of Chemistry and Institute for Sustainability and Energy at Northwestern, Northwestern University, Evanston, Illinois 60208, United States*

Daniel W. Houck − *McKetta Department of Chemical Engineering, Texas Materials Institute, The University of Texas at Austin, Austin, Texas 78712, United States;* orcid.org/0000-0002-3583-0595

Matthew S. Kirschner − *Department of Chemistry, Northwestern University, Evanston, Illinois 60208, United States*

Nathan C. Flanders − *Department of Chemistry, Northwestern University, Evanston, Illinois 60208, United States*

Alexandra Brumberg − *Department of Chemistry, Northwestern University, Evanston, Illinois 60208, United States;* orcid.org/0000-0003-2512-4686

Ariel A. Leonard − *Department of Chemistry, Northwestern University, Evanston, Illinois 60208, United States; Chemical Science and Engineering, Argonne National Laboratory, Lemont, Illinois 60439, United States*

Nicolas E. Watkins − *Department of Chemistry, Northwestern University, Evanston, Illinois 60208, United States*

Lin X. Chen − *Department of Chemistry, Northwestern University, Evanston, Illinois 60208, United States; Chemical Science and Engineering, Argonne National Laboratory, Lemont, Illinois 60439, United States*

William R. Dichtel − *Department of Chemistry, Northwestern University, Evanston, Illinois 60208, United States;* orcid.org/0000-0002-3635-6119

Xiaoyi Zhang − *X-ray Science Division, Argonne National Laboratory, Lemont, Illinois 60439, United States;* orcid.org/0000-0001-9732-1449

Brian A. Korgel − *McKetta Department of Chemical Engineering, Texas Materials Institute, The University of Texas at Austin, Austin, Texas 78712, United States;* orcid.org/0000-0001-6242-7526

Michael R. Wasielewski − *Department of Chemistry and Institute for Sustainability and Energy at Northwestern, Northwestern University, Evanston, Illinois 60208, United States;* orcid.org/0000-0003-2920-5440

Complete contact information is available at:
https://pubs.acs.org/10.1021/acsnano.0c05553

Notes

The authors declare no competing financial interest.

ACKNOWLEDGMENTS

We acknowledge student support from the National Science Foundation Macromolecular, Supramolecular, and Nanochemistry Program, NSF CHE 1808590. This work was supported by the National Science Foundation Graduate Research Fellowship Program under Grant DGE-1842165 (S.M.H., A.B., N.E.W.). We acknowledge support from the Ultrafast Initiative of the U.S. Department of Energy, Office of Science, Office of Basic Energy Sciences, through Argonne National Laboratory under Contract DE-AC02-06CH11357. B.A.K and D.W.H. acknowledge support from the Robert A. Welch Foundation (F-1464) and the National Science Foundation (IIP-182206 and IIP-1540028). Parts of this work were performed at the DuPont-Northwestern-Dow Collaborative Access Team (DND-CAT) located at Sector 5 of the Advanced Photon Source (APS). DND-CAT is supported by Northwestern University, E.I. DuPont de Nemours & Co., and the Dow Chemical Company. N.C.F. and L.X.C. are partially supported by Basic Energy Science, CBG Division, US Department of Energy through Argonne National Laboratory under Contract DE-AC02-06CH11357. N.C.F., R.R.L., and W.R.D. are partially supported by the Army Research Office for a Multidisciplinary University Research Initiatives (MURI) award under Grant W911NF-15-1-0447. This work was supported by the U.S. Department of Energy, Office of Science, Office of Basic Energy Sciences under Award DE-FG02-99ER14999 (M.R.W.). This work was performed, in part, at the Center for Nanoscale Materials and the Advanced Photon Source, both U.S. Department of Energy, Office of Science User Facilities, and supported by the U.S. Department of Energy, Office of Science, under Contract DE-AC02-06CH11357.

REFERENCES

(1) Coe, S.; Woo, W.-K.; Bawendi, M.; Bulović, V. Electroluminescence from Single Monolayers of Nanocrystals in Molecular Organic Devices. *Nature* **2002**, *420*, 800−803.
(2) Stolle, C. J.; Harvey, T. B.; Korgel, B. A. Nanocrystal Photovoltaics: A Review of Recent Progress. *Curr. Opin. Chem. Eng.* **2013**, *2*, 160−167.
(3) Murray, C. B.; Kagan, C. R.; Bawendi, M. G. Synthesis and Characterization of Monodisperse Nanocrystals and Close-Packed Nanocrystal Assemblies. *Annu. Rev. Mater. Sci.* **2000**, *30*, 545−610.
(4) Boles, M. A.; Engel, M.; Talapin, D. V. Self-Assembly of Colloidal Nanocrystals: From Intricate Structures to Functional Materials. *Chem. Rev.* **2016**, *116*, 11220−11289.
(5) Wang, Y.; Fedin, I.; Zhang, H.; Talapin, D. V. Direct Optical Lithography of Functional Inorganic Nanomaterials. *Science* **2017**, *357*, 385−388.
(6) Choi, J.-H.; Wang, H.; Oh, S. J.; Paik, T.; Sung, P.; Sung, J.; Ye, X.; Zhao, T.; Diroll, B. T.; Murray, C. B.; Kagan, C. R. Exploiting the Colloidal Nanocrystal Library to Construct Electronic Devices. *Science* **2016**, *352*, 205.
(7) Pietryga, J. M.; Park, Y.-S.; Lim, J.; Fidler, A. F.; Bae, W. K.; Brovelli, S.; Klimov, V. I. Spectroscopic and Device Aspects of Nanocrystal Quantum Dots. *Chem. Rev.* **2016**, *116*, 10513−10622.
(8) Wheeler, D. A.; Zhang, J. Z. Exciton Dynamics in Semiconductor Nanocrystals. *Adv. Mater.* **2013**, *25*, 2878−2896.
(9) Goldstein, A. N.; Echer, C. M.; Alivisatos, A. P. Melting in Semiconductor Nanocrystals. *Science* **1992**, *256*, 1425−1427.
(10) Lu, H. M.; Jiang, Q. Size-Dependent Surface Energies of Nanocrystals. *J. Phys. Chem. B* **2004**, *108*, 5617−5619.
(11) Magomedov, M. N. Dependence of the Surface Energy on the Size and Shape of a Nanocrystal. *Phys. Solid State* **2004**, *46*, 954−968.
(12) Alivisatos, A. P. Perspectives on the Physical Chemistry of Semiconductor Nanocrystals. *J. Phys. Chem.* **1996**, *100*, 13226−13239.
(13) Wills, A. W.; Kang, M. S.; Khare, A.; Gladfelter, W. L.; Norris, D. J. Thermally Degradable Ligands for Nanocrystals. *ACS Nano* **2010**, *4*, 4523−4530.
(14) Bucherl, C. N.; Oleson, K. R.; Hillhouse, H. W. Thin Film Solar Cells from Sintered Nanocrystals. *Curr. Opin. Chem. Eng.* **2013**, *2*, 168−177.
(15) Shamsi, J.; Rastogi, P.; Caligiuri, V.; Abdelhady, A. L.; Spirito, D.; Manna, L.; Krahne, R. Bright-Emitting Perovskite Films by Large-Scale Synthesis and Photoinduced Solid-State Transformation of $CsPbBr_3$ Nanoplatelets. *ACS Nano* **2017**, *11*, 10206−10213.
(16) Panthani, M. G.; Kurley, J. M.; Crisp, R. W.; Dietz, T. C.; Ezzyat, T.; Luther, J. M.; Talapin, D. V. High Efficiency Solution Processed Sintered CdTe Nanocrystal Solar Cells: The Role of Interfaces. *Nano Lett.* **2014**, *14*, 670−675.
(17) Stolle, C. J.; Harvey, T. B.; Korgel, B. A. Photonic Curing of Ligand-Capped $CuInSe_2$ Nanocrystal Films. In *Proceedings of the 2014 IEEE 40th Photovoltaic Specialist Conference (PVSC)*; Denver, June 8−13, 2004 ; IEEE: Piscataway, NJ, 2014; pp 0270−0274.
(18) Klimov, V. I.; McBranch, D. W.; Leatherdale, C. A.; Bawendi, M. G. Electron and Hole Relaxation Pathways in Semiconductor Quantum Dots. *Phys. Rev. B: Condens. Matter Mater. Phys.* **1999**, *60*, 13740−13749.
(19) Guyot-Sionnest, P.; Shim, M.; Matranga, C.; Hines, M. Intraband Relaxation in CdSe Quantum Dots. *Phys. Rev. B: Condens. Matter Mater. Phys.* **1999**, *60*, R2181−R2184.
(20) Klimov, V. I.; Mikhailovsky, A. A.; McBranch, D. W.; Leatherdale, C. A.; Bawendi, M. G. Quantization of Multiparticle Auger Rates in Semiconductor Quantum Dots. *Science* **2000**, *287*, 1011−1013.
(21) Efros, A., Auger Processes in Nanosize Semiconductor Crystals. In *Semiconductor Nanocrystals: From Basic Principles to Applications*, Efros, A. L., Lockwood, D. J., Tsybeskov, L., Eds.; Springer: Boston, MA, 2003; pp 52−72.
(22) Harvey, S. M.; Phelan, B. T.; Hannah, D. C.; Brown, K. E.; Young, R. M.; Kirschner, M. S.; Wasielewski, M. R.; Schaller, R. D. Auger Heating and Thermal Dissipation in Zero-Dimensional CdSe Nanocrystals Examined Using Femtosecond Stimulated Raman Spectroscopy. *J. Phys. Chem. Lett.* **2018**, *9*, 4481−4487.
(23) Diroll, B. T.; Kirschner, M. S.; Guo, P.; Schaller, R. D. Optical and Physical Probing of Thermal Processes in Semiconductor and Plasmonic Nanocrystals. *Annu. Rev. Phys. Chem.* **2019**, *70*, 353−377.
(24) Achermann, M.; Bartko, A. P.; Hollingsworth, J. A.; Klimov, V. I. The Effect of Auger Heating on Intraband Carrier Relaxation in Semiconductor Quantum Rods. *Nat. Phys.* **2006**, *2*, 557.
(25) Kittel, C., Semiconductor Crystals. In *Introduction to Solid State Physics*, 8th ed.; Wiley: New York, 1986; pp 185−220.
(26) Madelung, O., I-III-VI_2 Compounds. In *Semiconductors: Data Handbook*. Springer: Berlin, 2004; pp 289−328.
(27) Panthani, M. G.; Akhavan, V.; Goodfellow, B.; Schmidtke, J. P.; Dunn, L.; Dodabalapur, A.; Barbara, P. F.; Korgel, B. A. Synthesis of $CuInS_2$, $CuInSe_2$, and $Cu(In_xGa_{1-x})Se_2$ (CIGS) Nanocrystal "Inks" for Printable Photovoltaics. *J. Am. Chem. Soc.* **2008**, *130*, 16770−16777.
(28) Lim, Y. S.; Kwon, H.-S.; Jeong, J.; Kim, J. Y.; Kim, H.; Ko, M. J.; Jeong, U.; Lee, D.-K. Colloidal Solution-Processed $CuInSe_2$ Solar Cells with Significantly Improved Efficiency up to 9% by Morphological Improvement. *ACS Appl. Mater. Interfaces* **2014**, *6*, 259−267.
(29) Reiss, P.; Carrière, M.; Lincheneau, C.; Vaure, L.; Tamang, S. Synthesis of Semiconductor Nanocrystals, Focusing on Nontoxic and Earth-Abundant Materials. *Chem. Rev.* **2016**, *116*, 10731−10819.

(30) Kemell, M.; Ritala, M.; Leskelä, M. Thin Film Deposition Methods for $CuInSe_2$ Solar Cells. *Crit. Rev. Solid State Mater. Sci.* **2005**, *30*, 1−31.
(31) Akhavan, V. A.; Goodfellow, B. W.; Panthani, M. G.; Reid, D. K.; Hellebusch, D. J.; Adachi, T.; Korgel, B. A. Spray-Deposited $CuInSe_2$ Nanocrystal Photovoltaics. *Energy Environ. Sci.* **2010**, *3*, 1600−1606.
(32) Voggu, V. R.; Sham, J.; Pfeffer, S.; Pate, J.; Fillip, L.; Harvey, T. B.; Brown, R. M.; Korgel, B. A. Flexible $CuInSe_2$ Nanocrystal Solar Cells on Paper. *ACS Energy Lett.* **2017**, *2*, 574−581.
(33) Kergommeaux, A. d.; Fiore, A.; Faure-Vincent, J.; Pron, A.; Reiss, P. Colloidal $CuInSe_2$ Nanocrystals Thin Films of Low Surface Roughness. *Adv. Nat. Sci.: Nanosci. Nanotechnol.* **2013**, *4*, 015004.
(34) Stolle, C. J.; Harvey, T. B.; Pernik, D. R.; Hibbert, J. I.; Du, J.; Rhee, D. J.; Akhavan, V. A.; Schaller, R. D.; Korgel, B. A. Multiexciton Solar Cells of $CuInSe_2$ Nanocrystals. *J. Phys. Chem. Lett.* **2014**, *5*, 304−309.
(35) Harvey, T. B.; Mori, I.; Stolle, C. J.; Bogart, T. D.; Ostrowski, D. P.; Glaz, M. S.; Du, J.; Pernik, D. R.; Akhavan, V. A.; Kesrouani, H.; Vanden Bout, D. A.; Korgel, B. A. Copper Indium Gallium Selenide (CIGS) Photovoltaic Devices Made Using Multistep Selenization of Nanocrystal Films. *ACS Appl. Mater. Interfaces* **2013**, *5*, 9134−9140.
(36) AbuShama, J.; Noufi, R.; Johnston, S.; Ward, J.; Wu, X., Improved Performance in $CuInSe_2$ and Surface-Modified $CuGaSe_2$ Solar Cells. In *Proceedings of the 2004 DOE Solar Energy Technologies Program Review Meeting*; October 25−28, 2004 ; Office of Scientific & Technical Information Technical Reports, Department of Energy: Oak Ridge, TN, 2005; pp 299−302.
(37) Li, W.; Pan, Z.; Zhong, X. $CuInSe_2$ and $CuInSe_2$−ZnS Based High Efficiency "Green" Quantum Dot Sensitized Solar Cells. *J. Mater. Chem. A* **2015**, *3*, 1649−1655.
(38) Akkerman, Q. A.; Gandini, M.; Di Stasio, F.; Rastogi, P.; Palazon, F.; Bertoni, G.; Ball, J. M.; Prato, M.; Petrozza, A.; Manna, L. Strongly Emissive Perovskite Nanocrystal Inks for High-Voltage Solar Cells. *Nat. Energy* **2017**, *2*, 16194.
(39) Akhavan, V. A.; Harvey, T. B.; Stolle, C. J.; Ostrowski, D. P.; Glaz, M. S.; Goodfellow, B. W.; Panthani, M. G.; Reid, D. K.; Vanden Bout, D. A.; Korgel, B. A. Influence of Composition on the Performance of Sintered $Cu(In,Ga)Se_2$ Nanocrystal Thin-Film Photovoltaic Devices. *ChemSusChem* **2013**, *6*, 481−486.
(40) Nag, A.; Kovalenko, M. V.; Lee, J.-S.; Liu, W.; Spokoyny, B.; Talapin, D. V. Metal-Free Inorganic Ligands for Colloidal Nanocrystals: S^{2-}, HS^-, Se^{2-}, HSe^-, Te^{2-}, HTe^-, TeS_3^{2-}, OH^-, and NH_2^- as Surface Ligands. *J. Am. Chem. Soc.* **2011**, *133*, 10612−10620.
(41) Kovalenko, M. V.; Scheele, M.; Talapin, D. V. Colloidal Nanocrystals with Molecular Metal Chalcogenide Surface Ligands. *Science* **2009**, *324*, 1417.
(42) Stolle, C. J.; Panthani, M. G.; Harvey, T. B.; Akhavan, V. A.; Korgel, B. A. Comparison of the Photovoltaic Response of Oleylamine and Inorganic Ligand-Capped $CuInSe_2$ Nanocrystals. *ACS Appl. Mater. Interfaces* **2012**, *4*, 2757−2761.
(43) Tang, J.; Kemp, K. W.; Hoogland, S.; Jeong, K. S.; Liu, H.; Levina, L.; Furukawa, M.; Wang, X.; Debnath, R.; Cha, D.; Chou, K. W.; Fischer, A.; Amassian, A.; Asbury, J. B.; Sargent, E. H. Colloidal-Quantum-Dot Photovoltaics Using Atomic-Ligand Passivation. *Nat. Mater.* **2011**, *10*, 765−771.
(44) Kirschner, M. S.; Diroll, B. T.; Guo, P.; Harvey, S. M.; Helweh, W.; Flanders, N. C.; Brumberg, A.; Watkins, N. E.; Leonard, A. A.; Evans, A. M.; Wasielewski, M. R.; Dichtel, W. R.; Zhang, X.; Chen, L. X.; Schaller, R. D. Photoinduced, Reversible Phase Transitions in All-Inorganic Perovskite Nanocrystals. *Nat. Commun.* **2019**, *10*, 504.
(45) Kirschner, M. S.; Hannah, D. C.; Diroll, B. T.; Zhang, X.; Wagner, M. J.; Hayes, D.; Chang, A. Y.; Rowland, C. E.; Lethiec, C. M.; Schatz, G. C.; Chen, L. X.; Schaller, R. D. Transient Melting and Recrystallization of Semiconductor Nanocrystals under Multiple Electron−Hole Pair Excitation. *Nano Lett.* **2017**, *17*, 5314−5320.
(46) Houck, D. W.; Korgel, B. A. Facile Exchange of Tightly Bonded L-Type Oleylamine and Diphenylphosphine Ligands on Copper Indium Diselenide Nanocrystals Mediated by Molecular Iodine. *Chem. Mater.* **2018**, *30*, 8359−8367.
(47) Jain, A.; Ong, S. P.; Hautier, G.; Chen, W.; Richards, W. D.; Dacek, S.; Cholia, S.; Gunter, D.; Skinner, D.; Ceder, G.; Persson, K. A. Commentary: The Materials Project: A Materials Genome Approach to Accelerating Materials Innovation. *APL Mater.* **2013**, *1*, 011002.
(48) Szilagyi, E.; Wittenberg, J. S.; Miller, T. A.; Lutker, K.; Quirin, F.; Lemke, H.; Zhu, D.; Chollet, M.; Robinson, J.; Wen, H.; Sokolowski-Tinten, K.; Lindenberg, A. M. Visualization of Nanocrystal Breathing Modes at Extreme Strains. *Nat. Commun.* **2015**, *6*, 6577.
(49) Hannah, D. C.; Dunn, N. J.; Ithurria, S.; Talapin, D. V.; Chen, L. X.; Pelton, M.; Schatz, G. C.; Schaller, R. D. Observation of Size-Dependent Thermalization in CdSe Nanocrystals Using Time-Resolved Photoluminescence Spectroscopy. *Phys. Rev. Lett.* **2011**, *107*, 177403.
(50) Hannah, D. C.; Brown, K. E.; Young, R. M.; Wasielewski, M. R.; Schatz, G. C.; Co, D. T.; Schaller, R. D. Direct Measurement of Lattice Dynamics and Optical Phonon Excitation in Semiconductor Nanocrystals Using Femtosecond Stimulated Raman Spectroscopy. *Phys. Rev. Lett.* **2013**, *111*, 107401.
(51) Sánchez-Bajo, F.; Cumbrera, F. L. The Use of the Pseudo-Voigt Function in the Variance Method of X-Ray Line-Broadening Analysis. *J. Appl. Crystallogr.* **1997**, *30*, 427−430.
(52) Paszkowicz, W.; Minikayev, R.; Piszora, P.; Trots, D.; Knapp, M.; Wojciechowski, T.; Bacewicz, R. Thermal Expansion of $CuInSe_2$ in the 11−1,073 K Range: An X-Ray Diffraction Study. *Appl. Phys. A: Mater. Sci. Process.* **2014**, *116*, 767−780.
(53) Krynetskiĭ, I. B.; Gizhevskiĭ, B. A.; Naumov, S. V.; Kozlov, E. A. Size Effect of the Thermal Expansion of Nanostructural Copper Oxide. *Phys. Solid State* **2008**, *50*, 756−758.
(54) Kuru, Y.; Wohlschlögel, M.; Welzel, U.; Mittemeijer, E. J. Crystallite Size Dependence of the Coefficient of Thermal Expansion of Metals. *Appl. Phys. Lett.* **2007**, *90*, 243113.
(55) Magomedov, M. Dependence of the Thermal Expansion Coefficient on the Size and Shape of Diamond, Silicon and Germanium Nanocrystals. *J. Surf. Invest.: X-Ray, Synchrotron Neutron Tech.* **2015**, *9*, 1213−1220.
(56) Plech, A.; Kotaidis, V.; Grésillon, S.; Dahmen, C.; von Plessen, G. Laser-Induced Heating and Melting of Gold Nanoparticles Studied by Time-Resolved X-Ray Scattering. *Phys. Rev. B: Condens. Matter Mater. Phys.* **2004**, *70*, 195423.
(57) Hannah, D. C.; Gezelter, J. D.; Schaller, R. D.; Schatz, G. C. Reverse Non-Equilibrium Molecular Dynamics Demonstrate That Surface Passivation Controls Thermal Transport at Semiconductor−Solvent Interfaces. *ACS Nano* **2015**, *9*, 6278−6287.
(58) Ong, W.-L.; Rupich, S. M.; Talapin, D. V.; McGaughey, A. J. H.; Malen, J. A. Surface Chemistry Mediates Thermal Transport in Three-Dimensional Nanocrystal Arrays. *Nat. Mater.* **2013**, *12*, 410.
(59) Yazdani, N.; Andermatt, S.; Yarema, M.; Farto, V.; Bani-Hashemian, M. H.; Volk, S.; Lin, W. M. M.; Yarema, O.; Luisier, M.; Wood, V. Charge Transport in Semiconductors Assembled from Nanocrystal Quantum Dots. *Nat. Commun.* **2020**, *11*, 2852.
(60) Smith, A. R.; Yoon, W.; Heuer, W. B.; Baril, S. I. M.; Boercker, J. E.; Tischler, J. G.; Foos, E. E. Effect of Ligand Structure on the Optical and Electronic Properties of Nanocrystalline PbSe Films. *J. Phys. Chem. C* **2012**, *116*, 6031−6037.
(61) Lee, H.; Yoon, D.-E.; Koh, S.; Kang, M. S.; Lim, J.; Lee, D. C. Ligands as a Universal Molecular Toolkit in Synthesis and Assembly of Semiconductor Nanocrystals. *Chem. Sci.* **2020**, *11*, 2318−2329.
(62) Jeon, S.; Ahn, J.; Kim, H.; Woo, H. K.; Bang, J.; Lee, W. S.; Kim, D.; Hossain, M. A.; Oh, S. J. Investigation of the Chemical Effect of Solvent During Ligand Exchange on Nanocrystal Thin Films for Wearable Sensor Applications. *J. Phys. Chem. C* **2019**, *123*, 11001−11010.

https://dx.doi.org/10.1021/acsnano.0c05553
ACS Nano 2020, 14, 13548−13556